Journal of
Materials Chemistry A

ROYAL SOCIETY
OF CHEMISTRY

PAPER

View Article Online
View Journal

Cite this: DOI: 10.1039/d5ta07025b

Unlocking liquid chemisorption in solid matrices: immobilized deep eutectic solvent-ZIF-8 composites for next-generation CO_2 capture

Yunsung Yoo,[a] Xiaoliang Wang,[a] Haomiao Xie,[a] Geun-Ho Han,[b]
Ji-Yoon Song,[a] Milad Ahmadi Khoshooei,[a] Kent O. Kirlikovali,[a]
Justin M. Notestein,[b] Edward H. Sargent[ae] and Omar K. Farha*[abcd]

Achieving net-zero emissions by 2050 requires scalable and durable CO_2 capture solutions, with direct air capture (DAC) gaining increasing prominence. Deep eutectic solvents (DESs) have emerged as promising candidates due to their strong chemisorptive properties, but their liquid-phase nature limits integration into solid systems. In this study, we introduce a solid–liquid hybrid approach by immobilizing [TEAB][TEPA]$_2$, a highly CO_2-reactive DES, onto various supports *via* non-covalent immobilization. This strategy induces solid-like behavior while retaining molecular-level reactivity of the DES. Among the supports including ZIF-8, zeolite Y, zirconia, and alumina, the [TEAB][TEPA]$_2$@ZIF-8-56% composite demonstrated promising CO_2 uptake capacity of 2.00 mmol g^{-1} adsorbent at 1 bar, 1.48 at 0.15 bar, 0.96 at 0.01 bar, and 0.59 at 0.4 mbar. Particularly, we can observe that the chemisorption capacity under 400 ppm conditions is successfully introduced into ZIF-8, whereas pristine ZIF-8 showed negligible uptake under these same conditions. Breakthrough experiments confirmed robust capture behavior under humid conditions. The composite exhibited excellent cycling stability over 100 capture-release cycles, supported by thermogravimetric analysis. *In situ* DRIFTS verified that the chemisorptive nature of the DES remained intact after immobilization. Additional characterization studies, including FTIR, PXRD, N_2 physisorption, and XPS depth profiling, revealed partial DES infiltration and strong interfacial interactions. Comparative results using alumina-based composites underscored the importance of microporosity in stability. These findings suggest that DES-MOF composites hold promise as carbon capture materials, bridging liquid-phase functionality and solid-state robustness.

Received 29th August 2025
Accepted 6th December 2025

DOI: 10.1039/d5ta07025b

rsc.li/materials-a

Introduction

Climate change, a phenomenon increasingly recognized as one of the most pressing global challenges, is now manifesting observable impacts across both ecosystems and human societies. The Intergovernmental Panel on Climate Change (IPCC) has emphasized the urgent need for immediate mitigation strategies. In its most recent report, the panel warned about the narrowing window of opportunity to avert severe climate consequences. In response, major greenhouse gas-emitting nations have ratified key international frameworks, including the 2015 Paris Agreement and the forthcoming commitments expected from the 29th Conference of the Parties (COP29) in Azerbaijan, with a shared objective of achieving net-zero carbon emissions by 2050.

In parallel with these policy efforts, the advancement of technologies aimed at reducing CO_2 emissions plays a pivotal role in meeting the net-zero carbon targets by 2050. Notably, carbon dioxide accounts for more than 70% of total greenhouse gas emissions, underscoring the need for effective mitigation strategies.[1–9] Among these, direct air capture (DAC) and carbon capture, utilization, and storage (CCUS) have emerged as two of the most promising approaches. Both rely on high-performance sorbent systems capable of capturing CO_2 over a wide concentration range—from ambient atmospheric levels (~400 ppm) to concentrated industrial streams (up to 40%). This versatility is crucial for addressing various carbon sources, including ambient air, flue gas, and gases from pre-combustion or other industrial processes.[10–12]

Currently, aqueous amine-based absorption represents the most established method for post-combustion CO_2 capture, offering high efficiency even at low CO_2 concentrations.

---

[a] *Department of Chemistry, Northwestern University, 2145 Sheridan Road, Evanston, Illinois 60208, USA. E-mail: o-farha@northwestern.edu*

[b] *Department of Chemical and Biological Engineering, Northwestern University, 2145 Sheridan Road, Evanston, Illinois 60208, USA*

[c] *International Institute of Nanotechnology, Northwestern University, 2145 Sheridan Road, Evanston, Illinois 60208, USA*

[d] *Paula M. Trienens Institute for Sustainability and Energy, Northwestern University, Evanston, Illinois 60208, USA*

[e] *Department of Electrical and Computer Engineering, Northwestern University, 2145 Sheridan Road, Evanston, Illinois 60208, USA*

However, its large-scale application is hindered by several drawbacks, including high regeneration energy requirements, thermal and oxidative degradation of amines, as well as toxicity and corrosion issues associated with their use.[11,13,14] To address these limitations, alternative sorbent materials have been extensively explored.[15–18] Among them, deep eutectic solvents (DESs)—eutectic mixtures formed through strong hydrogen bonding interactions between hydrogen bond acceptors (HBAs) and hydrogen bond donors (HBDs)—have emerged as promising liquid-phase CO_2 sorbents due to their tunable physicochemical properties, high thermal and chemical stability, negligible vapor pressure, and low-cost, facile synthesis routes.[19–22] In particular, amine-functionalized DESs can be systematically designed to incorporate active sites for chemisorption by selecting HBD and HBA components with strong affinities for CO_2, which can form carbamate, carbamic acid, or bicarbonate species upon CO_2 adsorption. Utilizing such molecular design strategies, a variety of DESs with enhanced CO_2 capture capacities have been reported.[19,20,23–27]

While the liquid nature of DESs makes them well-suited for absorption-based CO_2 capture, it also limits their application in adsorption-driven systems, such as solid-state DAC or CCUS, which typically rely on porous solid sorbents. To overcome this constraint, we investigated an alternative approach: immobilizing DESs onto solid supports to impart solid-like characteristics. This strategy aims to retain the chemisorption activity of DESs while enabling their integration into adsorption platforms traditionally dominated by solid sorbents. Beyond enhancing the functional versatility of DESs, this approach also has the potential to confer strong chemisorption capabilities to conventional adsorbents, which typically rely on relatively weaker physisorption interactions. Such hybrid systems may further improve CO_2 capture efficiency under ultra-dilute conditions (*e.g.*, ambient air). Although similar composite strategies have been explored using polymers, polyamines, alkanolamines, and ionic liquids, including supported ionic liquid membranes (SILMs) and catalysts (SILCs), only a limited number of studies have investigated DES-based composites tailored for DAC-level CO_2 capture.[28–39]

In this study, we developed a series of DES-functionalized solid composites using a non-covalent immobilization method. The DES selected for immobilization—composed of tetraethylammonium bromide (TEAB), tetraethylenepentamine (TEPA), and water, hereafter referred to as $[TEAB][TEPA]_2$—was chosen for its high density of chemisorption-active amine groups and previously demonstrated CO_2 capture performance in the liquid phase.[24] The immobilization of this amine-rich DES within solid hosts was carried out with two primary objectives: (1) to introduce chemically active CO_2-binding sites into otherwise inert solid frameworks and (2) to achieve a liquid-to-solid-like transition *via* physical confinement, thereby enabling the DES to operate as a solid-state CO_2 adsorbent.

Various solid supports with distinct physicochemical properties were employed, including zirconia (ZrO_2), alumina (Al_2O_3), zeolite Y, and nanosized ZIF-8, ranging from extremely low-porosity to BET surface areas of 1550 $m^2\ g^{-1}$. These materials were selected to systematically investigate how surface area, porosity, particle size, and hydrophilicity influence the sorption behavior of the resulting composites. Specifically, nanosized ZIF-8, ZrO_2, and Al_2O_3 were chosen to maximize interfacial contact with the DES phase and minimize diffusion lengths, thereby enhancing mass transfer and adsorption–desorption kinetics. These characteristics are especially advantageous under low CO_2 partial pressures at ambient conditions (~400 ppm), where rapid uptake and efficient utilization of active sites for chemisorption are essential. Accordingly, these supports served as optimal platforms for evaluating the effectiveness of the composite sorbent design, which aims to integrate the chemisorption capacity of amine-rich DESs with the structural benefits of solid adsorbents.

The $[TEAB][TEPA]_2$@support composites were synthesized *via* non-covalent immobilization and characterized using a range of physicochemical techniques. CO_2 capture performance was assessed through isotherm measurements and cyclic adsorption–desorption experiments, accompanied by the optimization of DES loading levels. Mechanistic insights were derived from isotherm model fitting, and *in situ* DRIFTS under CO_2 flow was conducted to probe the chemisorption behavior of the immobilized DES phase. To further elucidate host–guest interactions and the synergistic effects between the DES and solid support, a comprehensive set of analytical methods—including XPS depth profiling, PXRD, FTIR, TGA, and SEM-EDS—was employed. These techniques provided insight into the spatial distribution of the DES phase and revealed evidence of confined-phase behavior and interfacial synergy.

By synthesizing a composite through DES immobilization, chemisorptive functionalities are imparted to ZIF-8, which alone cannot capture CO_2 from ambient air due to its ultra-dilute concentration (~400 ppm). As a result, the CO_2 uptake capacity of the composite is significantly enhanced compared to that of pristine ZIF-8 under DAC-relevant conditions.

Overall, this study demonstrates that immobilizing a DES within a microporous host not only retains its chemisorption functionality but also imparts solid-like adsorption characteristics, offering a promising strategy to bridge liquid- and solid-phase CO_2 capture technologies across a range of CO_2 concentrations relevant to diverse carbon sources.

Experimental

Synthetic procedures

Synthesis of nanosized ZIF-8. Nanosized ZIF-8 was synthesized following a previously reported procedure with slight modifications.[40,41] Specifically, 1.05 g of $Zn(NO_3)_2\cdot 6H_2O$ and 2.34 g of 2-methylimidazole were each dissolved in 50 mL of methanol under stirring and sonication in separate 100 mL sealed Duran bottles. The two precursor solutions were then combined in a 250 mL sealed Duran bottle containing a magnetic stir bar and stirred vigorously at room temperature for 1 h. The resulting nanoparticles were collected by centrifugation at 8000 rpm for 15 min and washed three times with methanol. Each washing step involved soaking the sample for 6 h in fresh methanol, totaling 18 h of washing time. The final product was dried under vacuum at 85 °C overnight and is hereafter referred to as "as-synthesized ZIF-8."

Synthesis of $[TEAB][TEPA]_2$ (DES). $[TEAB][TEPA]_2$ was synthesized following a previously reported protocol with slight modifications.[24] In this system, tetraethylenepentamine (TEPA), a polyamine compound, acted as the hydrogen bond donor (HBD) to introduce additional CO_2 chemisorption sites, while tetraethylammonium bromide (TEAB) served as the hydrogen bond acceptor (HBA). Specifically, 5 g of TEAB (23.77 mmol) and 9 g of TEPA (47.54 mmol) were mixed at a 1 : 2 molar ratio, along with 6 g of deionized water to reduce the viscosity of the mixture. The resulting solution was stirred vigorously at 25 °C for 24 h until a homogeneous and transparent deep eutectic solvent was obtained.

Fabrication of $[TEAB][TEPA]_2$@support composites. $[TEAB][TEPA]_2$@support composites were prepared using a non-covalent immobilization method. Prior to immobilization, all solid supports were pre-activated to eliminate surface-adsorbed impurities. Specifically, as-synthesized ZIF-8 was activated under dynamic vacuum at 100 °C overnight, while zeolite Y, alumina and zirconia were activated at 200 °C for 5 h under the same vacuum conditions.

For immobilization, the synthesized $[TEAB][TEPA]_2$ was first diluted in methanol at a 1 : 10 (w/w) ratio and stirred vigorously at 25 °C for 1 h. Subsequently, 50 mg of each activated support (ZIF-8, zeolite Y, alumina and zirconia) was transferred to individual 1-dram vials. The prepared DES/methanol solution was added to each vial to achieve a $[TEAB][TEPA]_2$-to-support mass ratio of 2 : 1 (w/w). The mixtures were briefly sonicated (5 min) and then stirred vigorously at 25 °C for 12 h in sealed vials. After immobilization, methanol was removed *via* rotary evaporation at 50 °C under reduced pressure. The resulting composites were further activated under dynamic vacuum at 60 °C for 10 h prior to characterization.

For the best-performing composite, additional optimization of the immobilization conditions was performed by varying the $[TEAB][TEPA]_2$-to-support mass ratio (1 : 1, 2 : 1, and 3 : 1) and immobilization time (12, 18, and 24 h) at 25 °C.

Characterization. Full details of the characterization methods can be found in the ESI but are briefly summarized here. Powder X-ray diffraction (PXRD) was used to assess the crystalline structure and phase integrity of pristine supports and $[TEAB][TEPA]_2$@support composites. Measurements were carried out at the IMSERC facility (Northwestern University) using a STOE-STADI-P diffractometer equipped with a Ge monochromator and a MYTHEN 2 1K detector. Samples were sealed between polyimide tapes in a 3 mm metallic mask and scanned over a 2θ range of 1.5–70° using Cu $K\alpha_1$ radiation (λ = 1.5406 Å, 40 kV, 40 mA). Calibration was performed using a NIST-certified silicon standard (SRM 640d).

Fourier-transform infrared (FTIR) spectroscopy was used to verify DES immobilization. ATR-FTIR spectra were collected at room temperature using a Bruker Tensor 37 spectrometer with a KBr beam splitter. Spectra were acquired over the 4000–600 cm^{-1} range with 64 scans and a spectral resolution of 4 cm^{-1}.

Nitrogen adsorption–desorption isotherms were measured at 77 K using a Micromeritics 3Flex analyzer. Prior to measurement, ZIF-8 was activated at 100 °C overnight, and zeolite Y, alumina, and zirconia were activated at 200 °C for 5 h. Composites were degassed at 60 °C under dynamic vacuum for 10 h. Pore size distributions were calculated using density functional theory (DFT) assuming cylindrical pore geometry.

CO_2 adsorption isotherms were recorded at 25 °C over a pressure range of 0–1 bar using the same instrument. Samples were pretreated under the same conditions as for N_2 isotherms.

Thermogravimetric analysis (TGA) was conducted using a Discovery TGA5500 analyzer (TA Instruments) under a dry N_2 flow (25 mL min^{-1}). Samples were heated from room temperature to 800 °C at 5 °C min^{-1}. For cycling tests, 100 consecutive CO_2 capture-release cycles were performed by alternating between 15% CO_2/85% N_2 (30 °C, 30 min) and 100% N_2 (90 °C, 30 min) with a ramp rate of 5 °C min^{-1}.

X-ray photoelectron spectroscopy (XPS) was performed using a Nexsa G2 system (Thermo Fisher Scientific) with monochromated Al $K\alpha$ radiation (λ = 1486.6 eV, 400 μm spot size). Depth profiling was carried out using 2000 eV Ar^+ ion sputtering in 10 s intervals for 31 cycles. All binding energies were referenced to the C 1s peak at 284.8 eV.

Scanning electron microscopy (SEM) and energy-dispersive X-ray spectroscopy (EDS) were performed on a JEOL JSM-7900FLV field-emission SEM at the EPIC facility. Samples were mounted on aluminum stubs with conductive carbon tape and coated with a 9 nm layer of OsO_4 using an OPC60A osmium coater. Elemental mapping was carried out using AZtec software (Oxford Instruments).

Inductively coupled plasma-optical emission spectroscopy (ICP-OES) was conducted using an iCAP 7600 spectrometer (Thermo Fisher Scientific) to quantify zinc content. Samples were digested using microwave-assisted acid digestion at 180 °C for 10 min and analysed against calibration standards (2.5–20 ppm) in 3% HNO_3.

Breakthrough experiments were conducted using a Micromeritics BreakThrough Analyzer coupled with an OmniStar GSD 350 mass spectrometer (Pfeiffer Vacuum). The $[TEAB][TEPA]_2$@ZIF-8 composite was tested using a simulated CO_2/N_2 gas mixture (15 : 85 v/v) at a flow rate of 5 mL min^{-1} under dry and humid conditions (relative humidity = 50% and 90%).

In situ diffuse reflectance infrared Fourier transform spectroscopy (DRIFTS) was performed using a Nicolet iS50 FTIR spectrometer equipped with a liquid nitrogen-cooled MCT detector and a Harrick Scientific Praying Mantis accessory. Measurements were carried out under a 15% CO_2 flow at 20 mL min^{-1}.

During adsorption measurements, two CO_2 concentration regimes were employed. Equilibrium uptake and low-partial-pressure performance were quantified down to ~400 ppm CO_2 to assess DAC-relevant behavior, whereas cyclic stability, breakthrough-type kinetics, and *in situ* DRIFTS were performed under 15% CO_2 in N_2 in order to obtain reproducible mass-change signals, reliable gas-phase analysis, and sufficiently strong vibrational features for mechanistic interpretation.

Results and discussion

Synthesis and characterization of [TEAB][TEPA]$_2$@support composites

Each [TEAB][TEPA]$_2$@support composite was synthesized *via* non-covalent immobilization. After synthesis, the composites were dried, activated under dynamic vacuum, and subsequently used in powder form for all characterizations. Fig. 1 summarizes the characterization of both pristine supports and [TEAB][TEPA]$_2$@support composites, including FTIR spectra, PXRD patterns, and CO_2/N_2 adsorption isotherms. In all panels, composites are shown in darker colors and pristine supports in lighter shades of the same hue. FTIR analysis was used to confirm successful immobilization of [TEAB][TEPA]$_2$ within each support, and PXRD analysis was used to verify that the crystalline structure of the support was preserved after immobilization.

The FTIR spectra in Fig. 1(a) show that characteristic peaks of [TEAB][TEPA]$_2$ are present in all [TEAB][TEPA]$_2$@support composites, confirming immobilization of the DES. Specifically, bands at 3550–3200 cm^{-1} (O–H and N–H stretching), 2940 and 2835 cm^{-1} (asymmetric and symmetric C–H stretching in CH_3 and CH_2 groups), 1655 cm^{-1} (H_2O bending), 1600 cm^{-1} (N–H bending), 1500–1370 cm^{-1} (O–H and C–H bending in alkyl groups), and 784 cm^{-1} (C–N wagging) are attributable to [TEAB][TEPA]$_2$ and are clearly detected in the composites.

The PXRD patterns in Fig. 1(b) indicate that the crystalline structure of each support was largely retained after immobilization of [TEAB][TEPA]$_2$, although some diffraction peaks corresponding to crystalline TEAB were also detected.

Additionally, to evaluate the CO_2 capture capacity of the composites, adsorption isotherms were measured at 25 °C, as shown in Fig. 1(c). In all cases, the [TEAB][TEPA]$_2$@support composites exhibited a noticeable increase in CO_2 uptake at low

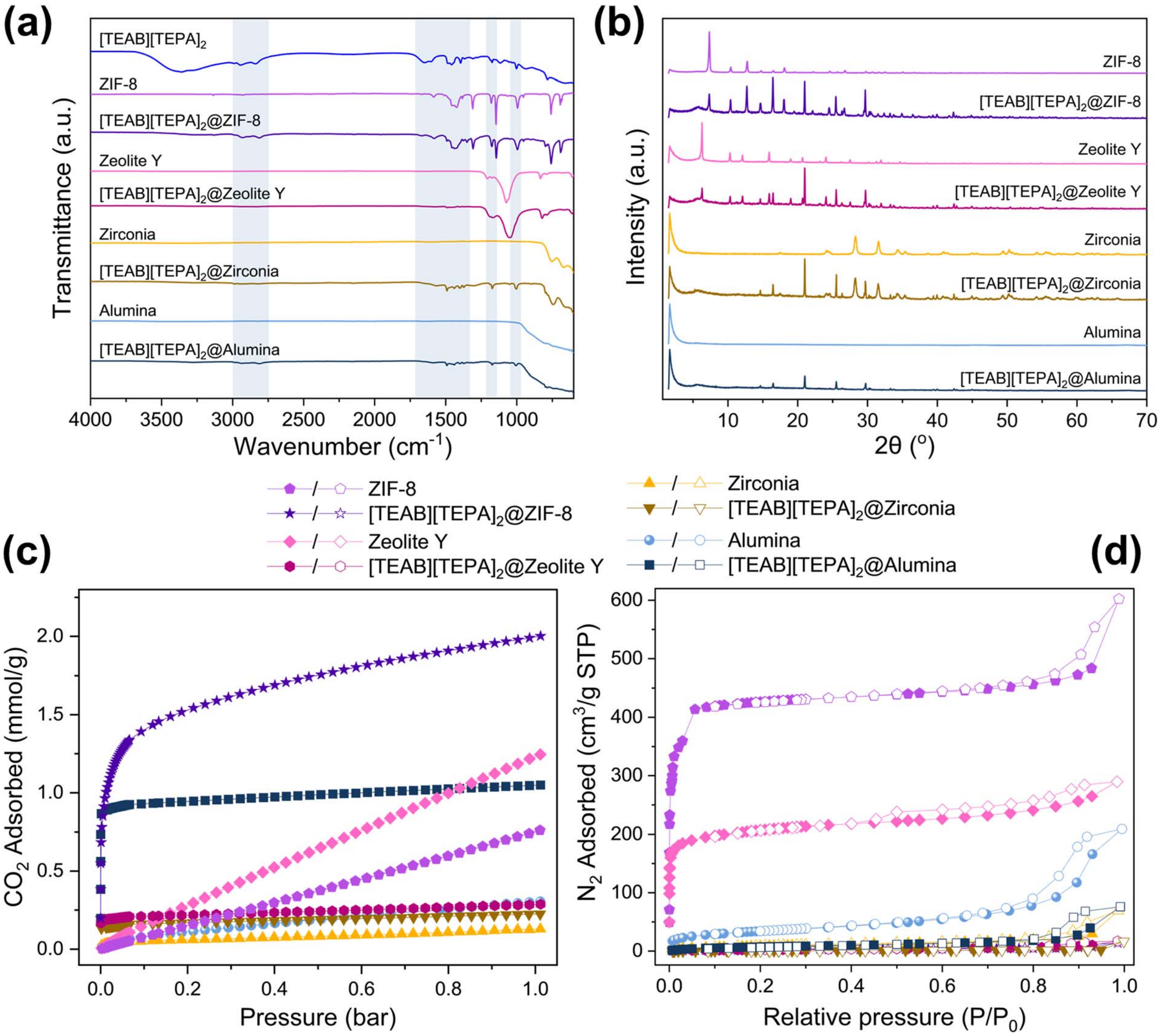

Fig. 1 (a) FTIR spectra and (b) PXRD patterns of pristine supports (ZIF-8, zeolite Y, zirconia, and alumina) and their corresponding [TEAB][TEPA]$_2$@support composites. (c) CO_2 adsorption isotherms at 298 K and (d) N_2 adsorption isotherms at 77 K for all samples. In all panels, composites are shown in darker colors and pristine supports in lighter colors of the same hue.

partial pressure (<0.05 bar), compared to their corresponding pristine supports. This result indicates that the incorporation of $[TEAB][TEPA]_2$ introduced additional chemisorption sites effective for capturing CO_2 at low concentrations.

The degree of enhancement, however, varied with the support. While $[TEAB][TEPA]_2$@zirconia showed only a modest increase in CO_2 uptake under low-pressure conditions, $[TEAB][TEPA]_2$@zeolite Y exhibited even lower CO_2 capacity than pristine zeolite Y at higher partial pressures.

In contrast, both $[TEAB][TEPA]_2$@alumina and $[TEAB][TEPA]_2$@ZIF-8 displayed significantly greater CO_2 capture capacity across the entire 0–1 bar range, suggesting that these two systems are particularly promising. Therefore, TGA-based cyclic stability analysis was performed exclusively on these two composites to explore the kinetics of CO_2 capture and release and to identify the optimal support-DES combinations.

Fig. 1(d) and Table 1 show the N_2 sorption isotherms and the corresponding textural properties, including BET area ($m^2\ g^{-1}$), total pore volume ($cm^3\ g^{-1}$), and micropore volume ($cm^3\ g^{-1}$). As illustrated in Fig. 1(d), all DES-loaded samples (darker curves) exhibited decreased N_2 uptake compared to their pristine counterparts (lighter curves), suggesting partial pore blockage or infiltration by the DES phase. This effect was most pronounced in ZIF-8, which showed a marked decrease in BET area and total pore volume, indicating that a large fraction of its micropores became inaccessible to nitrogen molecules under 77 K adsorption conditions following immobilization.

To compare the cyclic stability of $[TEAB][TEPA]_2$@ZIF-8 and $[TEAB][TEPA]_2$@alumina under realistic operating conditions, more than 100 CO_2 capture-release cycles were conducted using thermogravimetric analysis (TGA). Each cycle consisted of CO_2 adsorption under a 15% CO_2/85% N_2 gas stream at 30 °C for 30 min, followed by desorption at 90 °C under N_2, with a heating rate of 5 °C min^{-1}. As shown in Fig. 2, the initial CO_2 uptake during the first cycle closely matched the values obtained from the CO_2 isotherms, which confirmed consistency between gravimetric and volumetric measurements. However, as cycling progressed, distinct differences emerged between the two composites.

$[TEAB][TEPA]_2$@alumina, which is supported on a low-porosity substrate exhibited poor cycling performance. A 50% reduction in CO_2 uptake was already evident after just 25 cycles, and by cycle 75, the capacity approached that of pristine alumina—implying near-complete depletion of the DES phase. This result suggested the interaction between $[TEAB][TEPA]_2$ and the alumina surface was too weak to retain the DES during prolonged cycling.

In contrast, $[TEAB][TEPA]_2$@ZIF-8, which was supported on microporous ZIF-8, exhibited a 26.6% decrease in CO_2 uptake over the first 50 cycles, after which the capacity largely stabilized. Only a 0.43% additional loss was measured between cycles 50 and 100. This plateau suggests that $[TEAB][TEPA]_2$ was retained within the support, and the interaction between $[TEAB][TEPA]_2$ and the ZIF-8 framework was sufficiently strong to maintain long-term stability. Taken together, these results led us to hypothesize that partial infiltration of $[TEAB][TEPA]_2$ into the microporous ZIF-8 framework, along with favorable host–guest interactions, may have contributed to the enhanced cycling stability in the ZIF-8-based composite. In contrast, the absence of such interactions in the alumina-based system likely resulted in premature DES loss and poor reusability.

To further clarify the interactions between $[TEAB][TEPA]_2$ and the respective supports—and to support the proposed hypothesis of DES–ZIF-8 interaction and partial pore infiltration—XPS depth profiling was conducted on both $[TEAB][TEPA]_2$@ZIF-8 and $[TEAB][TEPA]_2$@Alumina. Snapshots of Zn $2p_{3/2}$, N 1s, O 1s, and Br 3d were collected for the ZIF-8-based composite, while Al 2p, N 1s, O 1s, and Br 3d spectra were obtained for the alumina-based sample, as shown in Fig. 3.

As the depth profiling progressed, the two systems showed distinct behavior. For $[TEAB][TEPA]_2$@Alumina, the spectra showed no significant binding energy shifts in any of the probed elements (Al, N, Br, and O), and only changes in peak intensity were detected with increasing etching depth. These results are consistent with limited specific interaction between $[TEAB][TEPA]_2$ and the alumina, agreed with the rapid capacity loss observed in the TGA cycling tests.

In contrast, $[TEAB][TEPA]_2$@ZIF-8 exhibited distinct shifts in the binding energies of Zn, N, and Br. Notably, both Zn $2p_{3/2}$ and N 1s spectra showed peak splitting, which implied changes in the local chemical environment. These spectral features suggest the presence of specific interactions between the DES and the ZIF-8 framework—such as Zn-N coordination—as well as partial confinement of the DES within the micropores. A

Table 1 Textural properties of pristine solid supports and their corresponding $[TEAB][TEPA]_2$@support composites

Materials	BET area ($m^2\ g^{-1}$)	Total pore volume ($cm^3\ g^{-1}$)	Micropore volume[a] ($cm^3\ g^{-1}$)
ZIF-8	1550	0.626	0.604
$[TEAB][TEPA]_2$@ZIF-8	8	0.006	—
Zeolite Y	787	0.32	0.234
$[TEAB][TEPA]_2$@Zeolite Y	10	0.003	—
Alumina	121	0.06	0.006
$[TEAB][TEPA]_2$@Alumina	28	0.013	—
Zirconia	33	0.004	—
$[TEAB][TEPA]_2$@Zirconia	3	0.0004	—

[a] Micropore volume was calculated using the *t*-plot method.

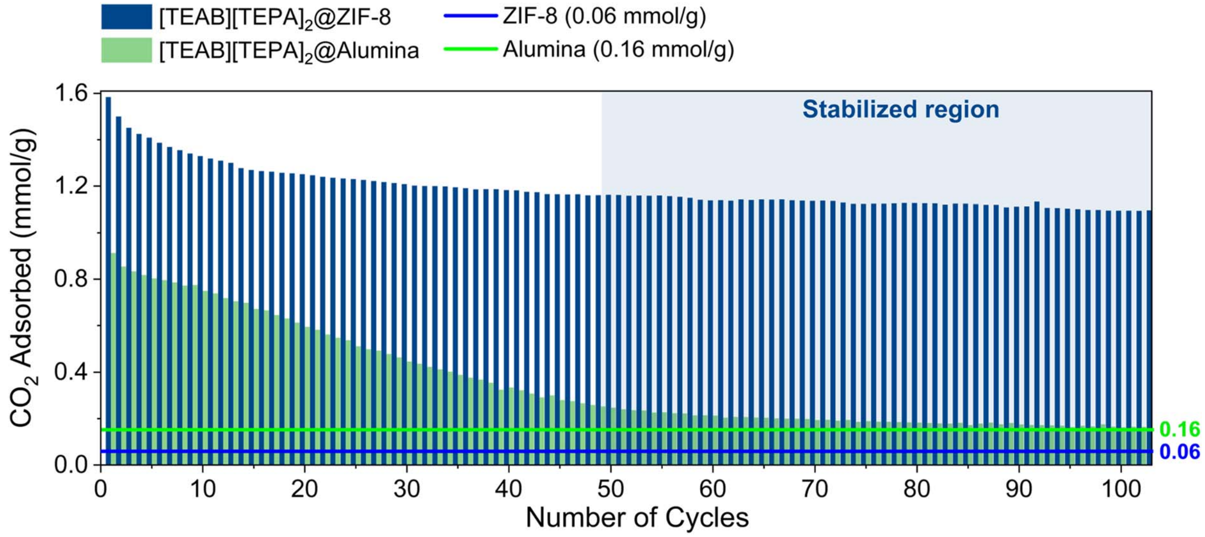

Fig. 2 Cyclic CO_2 capture–release performance of [TEAB][TEPA]$_2$@ZIF-8 and [TEAB][TEPA]$_2$@Alumina over 100 cycles in a binary CO_2/N_2 gas mixture (15/85, v/v). The CO_2 uptake of pristine alumina (0.16 mmol g^{-1}, green line) and ZIF-8 (0.06 mmol g^{-1}, blue line) are shown as reference materials. Each cycle consisted of a capture step under the same CO_2/N_2 mixture at 30 °C for 30 minutes, followed by a release step under 100% N_2 at 90 °C for 30 minutes, with a heating rate of 5 °C min^{-1}. The total gas flow rate was maintained at 25 mL min^{-1} throughout the entire process.

more detailed interpretation of these spectral shifts, along with additional characterization to verify the interactions, is provided in the section discussing the localization of [TEAB][TEPA]$_2$ within ZIF-8, where the spatial distribution of the deep eutectic solvent is thoroughly examined.

As a conclusion to the support screening phase, among the various solid supports evaluated—including nanosized alumina, zirconia, and zeolite Y—nanosized ZIF-8 demonstrated the most promising CO_2 capture performance, particularly under low CO_2 concentrations, as well as superior cyclic stability over 100 adsorption–desorption cycles. Based on these comparative insights, further optimization of the [TEAB][TEPA]$_2$@ZIF-8 composite was pursued by systematically varying two key variables of immobilization time and the mass ratio of DES used during immobilization.

Optimization of synthesis condition and characterization of [TEAB][TEPA]$_2$@ZIF-8 composites

To optimize the synthesis of [TEAB][TEPA]$_2$@ZIF-8 composites, two variables were systematically investigated: immobilization time (12, 18, and 24 h) and the mass ratio of [TEAB][TEPA]$_2$ to ZIF-8 (3 : 1, 2 : 1, and 1 : 1). Fig. 4 presents the characterization results for pristine ZIF-8 and nine synthesized composites, including FTIR, PXRD, and CO_2 adsorption isotherms at 25 °C.

FTIR and PXRD analyses were first performed to confirm successful immobilization of [TEAB][TEPA]$_2$ and to assess whether the ZIF-8 structure was preserved after loading. As shown in Fig. 4(a), the FTIR spectra of all composites displayed characteristic peaks corresponding to [TEAB][TEPA]$_2$, confirming successful loading. Notably, the intensity of these peaks increased with higher [TEAB][TEPA]$_2$ content, indicating higher DES loading. PXRD patterns in Fig. 4(b) confirmed that the crystalline structure of ZIF-8 was preserved across all composites regardless of immobilization time or DES ratio. Interestingly, with increasing DES content and time, the relative intensity of the ZIF-8 (011) peak at 7.3° decreased, while the (022) and (013) reflections at 14.8° and 16.4°, respectively, increased. Similar intensity redistribution had been reported in other MOF-solvent composite systems and was often interpreted as evidence of pore infiltration by polar species (*e.g.*, amines, ionic liquids).[28,30,32] However, such changes could also arise from surface deposition or pore blockage effects, so these patterns alone were not sufficient to prove internal infiltration.

CO_2 adsorption isotherms at 25 °C were then measured for all composites to identify the optimal synthesis condition for capture performance. Fig. 4(c) and (d) show the results plotted on linear and logarithmic pressure scales, respectively. All [TEAB][TEPA]$_2$@ZIF-8 composites outperformed pristine ZIF-8 over 0–1 bar, with especially pronounced improvements below 0.2 bar, indicating the successful introduction of additional chemisorption sites *via* DES incorporation. However, CO_2 uptake did not increase monotonically with increasing DES content, suggesting that optimal performance depends on a balanced interaction between the ZIF-8 framework and the DES phase. Among the tested conditions, [TEAB][TEPA]$_2$@ZIF-8 (2 : 1, 12 h) exhibited the highest CO_2 uptake, achieving 0.59, 0.96, 1.48, and 2.00 mmol g^{-1} at 0.4 mbar, 0.01, 0.15, and 1 bar, respectively. In contrast, pristine ZIF-8 showed uptake values of only 0.06, 0.11, and 0.76 mmol g^{-1} at 0.01, 0.15, and 1 bar, with no measurable adsorption at 0.4 mbar. These results represent approximately 16-fold and 13.5-fold enhancements at 0.01 and 0.15 bar, respectively, for the optimized composite—highlighting its superior performance particularly under low CO_2 partial pressures.

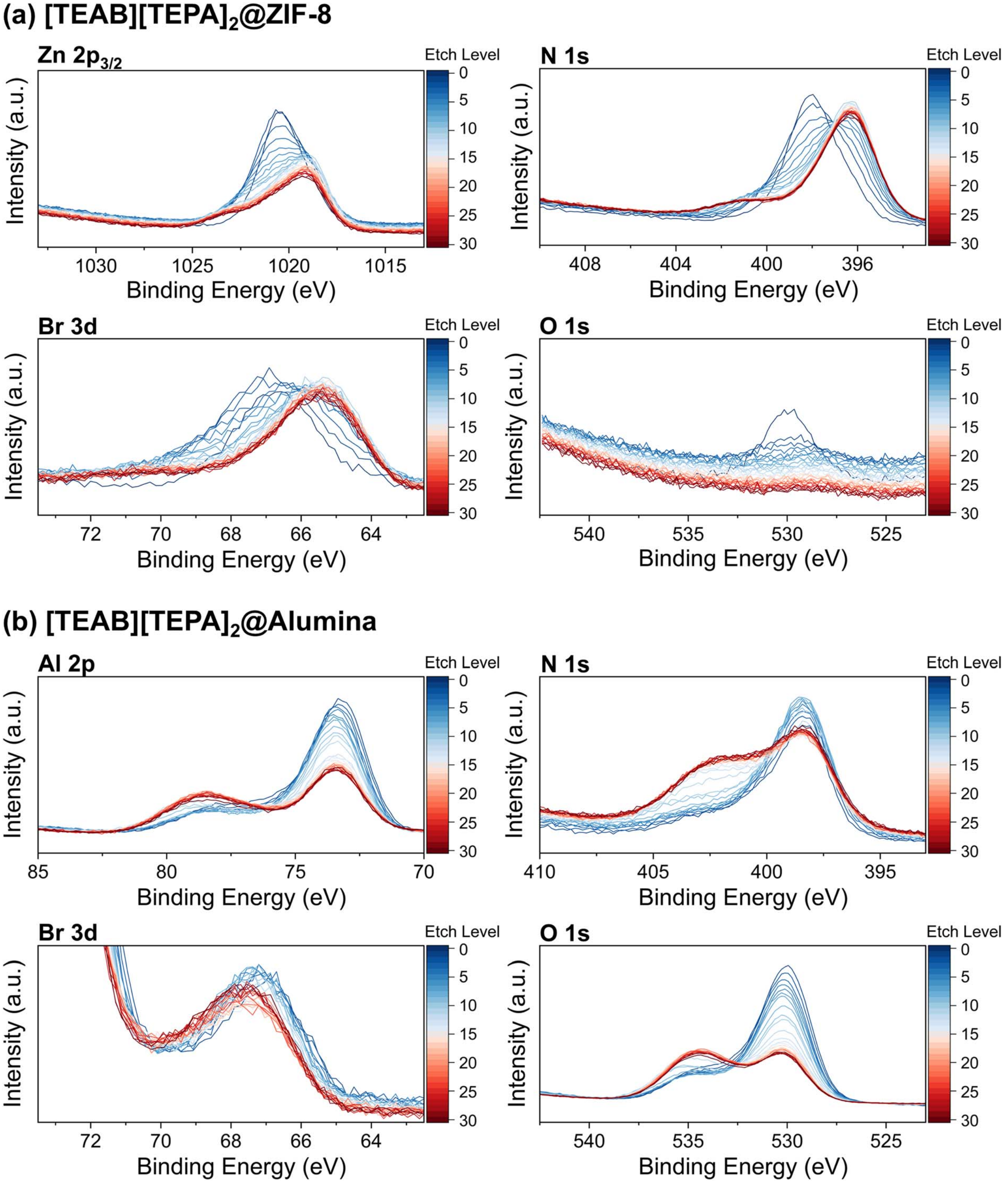

Fig. 3 XPS depth profiles of (a) [TEAB][TEPA]$_2$@ZIF-8 and (b) [TEAB][TEPA]$_2$@alumina, showing the evolution of Zn 2p$_{3/2}$ (ZIF-8), Al 2p (alumina), Br 3d, N 1s, and O 1s signals as a function of etch level. Depth profiling was conducted using monoatomic Ar$^+$ sputtering at 2000 eV in 10 s intervals per cycle, for a total of 31 etching cycles. All binding energies were referenced to the C 1s peak at 284.8 eV. Samples were mounted on adhesive copper tape and analyzed using monochromated Al Kα radiation ($\lambda = 1486.6$ eV) with a ∼400 μm spot size.

To investigate morphological changes induced by DES incorporation, SEM images were obtained (Fig. S1). Pristine ZIF-8 particles were approximately 50–80 nm in size, whereas the composites exhibited larger apparent particle sizes ranging from 100 to 250 nm, primarily due to the immobilization process. As the amount of [TEAB][TEPA]$_2$ and immobilization time increased, aggregation among ZIF-8 particles became more pronounced, contributing to a further increase in overall particle size. This trend was most evident in the [TEAB]

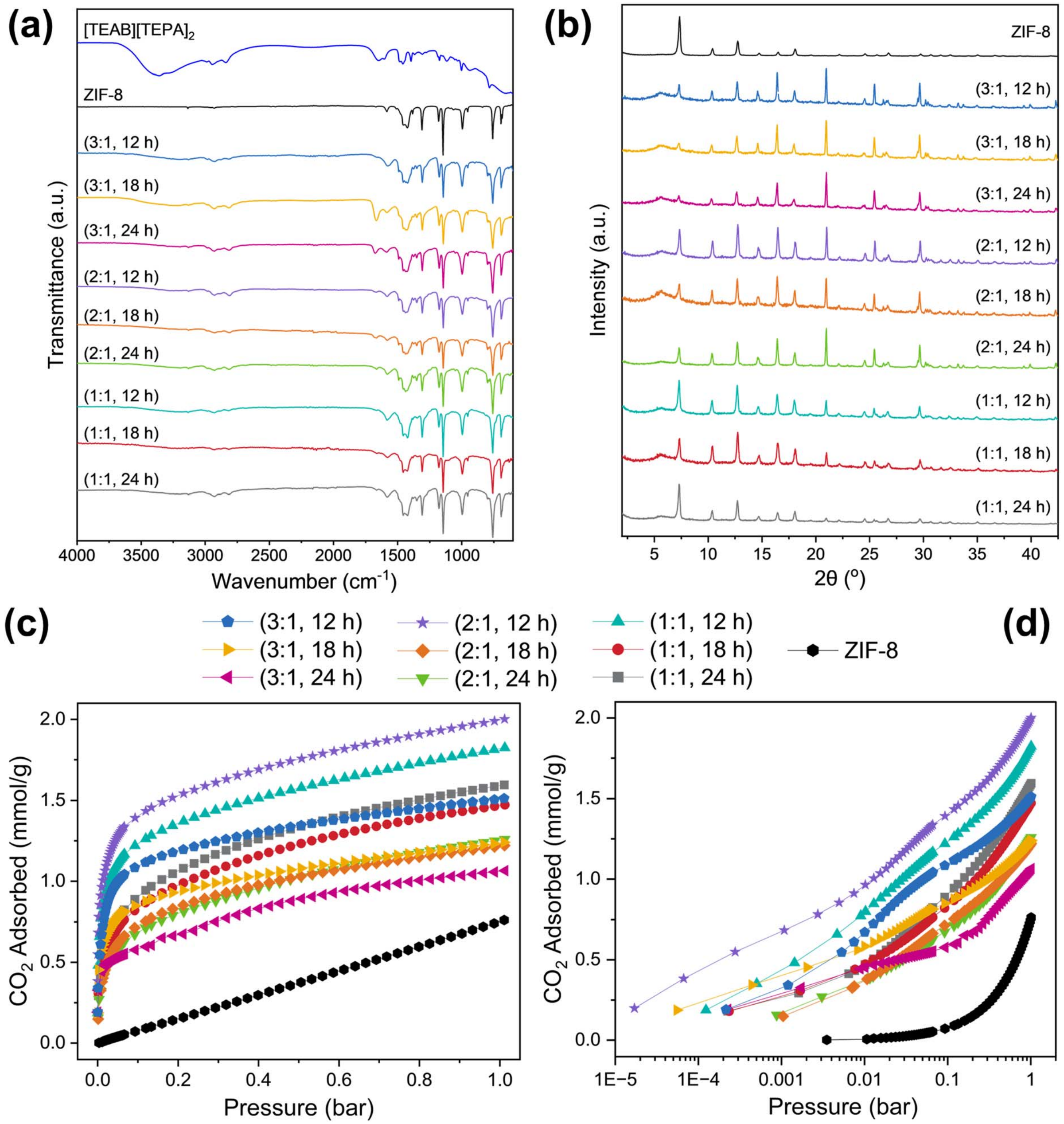

Fig. 4 (a) FTIR spectra and (b) PXRD patterns of ZIF-8 and [TEAB][TEPA]$_2$@ZIF-8 composites synthesized with varying [TEAB][TEPA]$_2$: ZIF-8 weight ratios (1 : 1, 2 : 1, and 3 : 1) and immobilization times (12, 18, and 24 h). (c and d) CO$_2$ adsorption isotherms at 298 K plotted in (c) linear and (d) logarithmic scale, highlighting the effect of synthesis conditions on CO$_2$ uptake behavior.

[TEPA]$_2$@ZIF-8 (3 : 1, 24 h) sample, which showed substantial aggregation and the largest average particle size.

Based on these findings, subsequent characterization efforts focused on the [TEAB][TEPA]$_2$@ZIF-8 (2 : 1, 12 h) composite to further investigate its structural, chemical, and sorption properties.

Additional characterization of the best-performing [TEAB][TEPA]$_2$@ZIF-8 composite

To quantify the [TEAB][TEPA]$_2$ content in the optimized composite, inductively coupled plasma-optical emission spectroscopy (ICP-OES) was performed to measure the zinc (Zn) content, which originates solely from ZIF-8. Pristine ZIF-8 and [TEAB][TEPA]$_2$@ZIF-8 (2 : 1, 12 h) contained 27.16 wt% and 11.95 wt% Zn, respectively. From these values, the ZIF-8 fraction in the composite was calculated to be approximately 44 wt%, corresponding to a [TEAB][TEPA]$_2$ loading of 56 wt%. Accordingly, this sample is hereafter referred to as [TEAB][TEPA]$_2$@-ZIF-8–56% throughout this study.

Thermogravimetric analysis (TGA) under N_2 was then performed to compare the thermal behavior of [TEAB][TEPA]$_2$@ZIF-8–56% with pristine ZIF-8 and to gain indirect insight into possible interactions between the two components. As shown in Fig. S2, pristine ZIF-8 did not exhibit any mass loss until ~550 °C, followed by a sharp decomposition between 550–650 °C corresponding to linker degradation and framework collapse. In contrast, [TEAB][TEPA]$_2$@ZIF-8–56% showed multi-step mass loss: initial loss below 150 °C due to water evaporation, and gradual decomposition between 150–500 °C attributed to thermal degradation of the DES components. Notably, no distinct collapse step near 630 °C was observed, suggesting a possible alteration in the Zn–N coordination environment induced by the presence of [TEAB][TEPA]$_2$. In addition, residual decomposition products may have acted as a thermal buffer, leading to the more gradual weight loss profile at elevated temperatures.

Additionally, SEM-EDS mapping was conducted on [TEAB][TEPA]$_2$@ZIF-8–56% to further evaluate the spatial distribution of Zn, Br, N and O elements (Fig. 5(a)). The elemental maps showed that Br was uniformly distributed in the same regions as Zn, indicating that the DES phase was evenly dispersed at the particle surface.

Following this, CO_2 capture behavior was examined for [TEAB][TEPA]$_2$@ZIF-8–56%. CO_2 adsorption isotherms of pristine ZIF-8 and the composite were fitted to classical adsorption models (Langmuir, dual-site Langmuir, Freundlich, and Sips), and the fitted curves and parameters are provided in Fig. S3(a) and Table S1. Pristine ZIF-8 exhibited nearly linear, Henry-like uptake over the investigated pressure range and was best described by a Freundlich-type response, whereas [TEAB][TEPA]$_2$@ZIF-8–56% was best described by a Sips-type response, consistent with pressure-dependent saturation on a heterogeneous adsorption surface (Fig. 3(b)). The specific contribution of the immobilized DES phase was then isolated by subtracting the ZIF-8 contribution from the composite isotherm and normalizing it by the known 56 wt% DES loading. This analysis showed that the immobilized DES maintained substantial CO_2 capacity across relevant CO_2 partial pressures, including dilute conditions down to ~400 ppm, where the uptake reached 1.02 mmol g^{-1} DES (Fig. S3(b)). This value corresponds to the estimated contribution of the DES phase itself based on model fitting, rather than the overall uptake of the composite under DAC conditions. Full details of the fitting procedure, the parameter constraints applied to avoid non-physical saturation behavior, and the quantitative differential analysis are provided in the SI.

Importantly, the immobilized DES exhibits solid-like behavior, acting as a microporous adsorbent rather than a liquid-phase absorbent. This observation underscores the potential of the DES-MOF composite as a promising candidate for direct air capture, pending further optimization of the composite formulation. The findings point to the potential of creating a heterogeneous composite structure, in which physically confined DES exhibits solid-state-like CO_2 adsorption

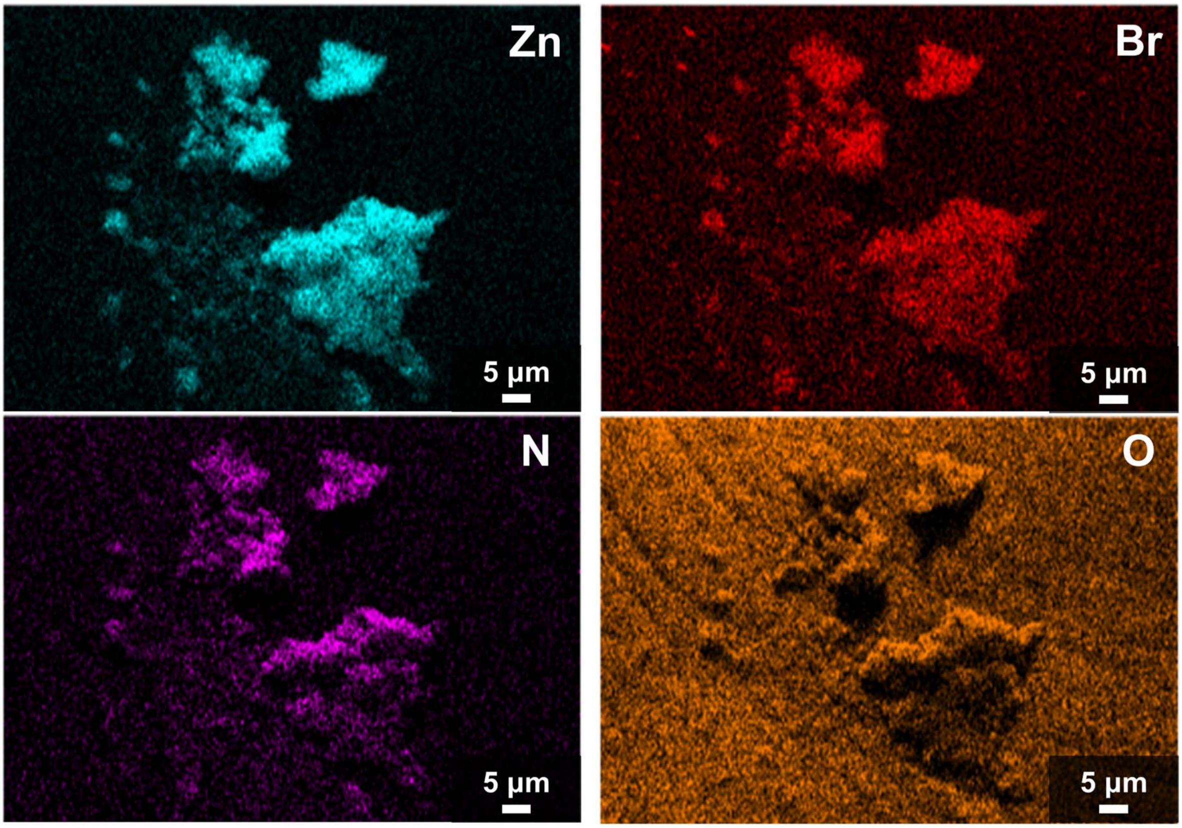

Fig. 5 SEM–EDS elemental mapping images of the [TEAB][TEPA]$_2$@ZIF-8 composite-56%, showing the spatial distribution of Zn, Br, N, and O elements.

characteristics while retaining high uptake at ambient conditions.

To further evaluate the CO_2 adsorption performance of [TEAB][TEPA]$_2$@ZIF-8–56% under dynamic conditions and in the presence of moisture, breakthrough experiments were conducted using a simulated CO_2/N_2 mixture (15 : 85 v/v) under both dry and humid environments (relative humidities of 50% and 90%). Fig. S4 presents the CO_2 and N_2 breakthrough curves over three consecutive cycles under dry conditions. Notably, no significant changes were observed in either the CO_2 (filled symbols, blue) or N_2 (hollow symbols, red) profiles throughout the cycles, demonstrating stable adsorption–desorption behavior. This observed cyclic stability is in good agreement with the durability confirmed by 100 consecutive CO_2 capture-release cycles in TGA, together highlighting the reliable reusability of the composite under dynamic operating conditions.

Fig. 6 compares the breakthrough behavior of the composite under dry (blue), 50% RH (red), and 90% RH (green) conditions. Under dry conditions, the composite exhibited a CO_2 uptake of 0.934 mmol g^{-1}, with a breakthrough time of 22.9 min g^{-1} ($C/C_0 = 0.05$) and a saturation time of 55.7 min g^{-1} ($C/C_0 = 0.99$). Remarkably, even under humid conditions, the composite maintained high CO_2 uptake capacities of 0.748 and 0.734 mmol g^{-1} composite at 50% and 90% RH, respectively, thereby retaining 80.1% and 78.6% of the dry-state performance. Corresponding breakthrough times were slightly shortened to 17.4 and 16.6 min g^{-1}, while saturation times remained reasonably long at 45.1 and 48.1 min g^{-1}.

These results confirm that the immobilized DES phase retains its chemisorptive functionality even in humid environments, delivering robust CO_2 capture performance under realistic gas compositions. The slight reduction in breakthrough and saturation times under humid conditions may reflect minor competitive adsorption effects from water vapor. Nonetheless, the composite demonstrates outstanding applicability for practical CO_2 separation processes, including direct air capture, under ambient and moisture-rich conditions.

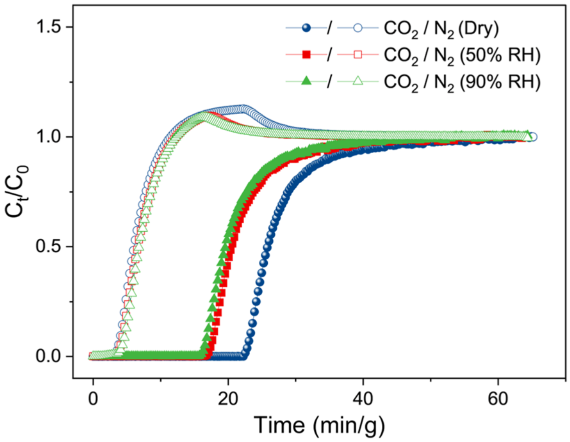

Fig. 6 Breakthrough curves of [TEAB][TEPA]$_2$@ZIF-8-56% under a binary CO_2/N_2 gas mixture (15/85, v/v) at varying humidity levels: dry (blue), 50% RH (red), and 90% RH (green), illustrating humidity-dependent adsorption performance. The total gas flow rate was maintained at 5 mL min^{-1}.

In situ DRIFTS analysis was performed under 15% CO_2 flow at 25 °C for 30 minutes to investigate the CO_2 chemisorption mechanism and evaluate whether the chemisorptive properties of [TEAB][TEPA]$_2$ were retained in the composite. Fig. S5(a) and (b) show the time-resolved spectra in Kubelka–Munk units, corresponding to two spectral regions: 3800–2900 cm^{-1} and 2600–1100 cm^{-1}, respectively. To facilitate a more intuitive interpretation of the spectral evolution, Fig. 7 presents color maps spanning the full wavenumber range from 4000 to 800 cm^{-1}.

In the high wavenumber region (3800–2900 cm^{-1}), the emergence and gradual increase of distinct O–H stretching bands was observed. Specifically, sharp peaks at 3728 and 3700 cm^{-1} were assigned to asymmetric stretching of free O–H groups, while peaks at 3625 and 3597 cm^{-1} correspond to symmetric free and weakly hydrogen-bonded O–H stretching modes, respectively. These features are primarily attributed to water molecules inherently present in the DES phase and suggest water's active involvement in CO_2 chemisorption *via* proton transfer, intermediate stabilization, and potential bicarbonate formation pathways—similar to mechanisms observed in aqueous amine systems.[42–44] Alongside these, broadening and intensity increases at 3432 and 3340 cm^{-1} were assigned to asymmetric and symmetric N–H stretching of primary amines, while features near 3250–3200 cm^{-1} were attributed to secondary amine N–H and strongly hydrogen-bonded O–H stretches. These concurrent changes suggest progressive CO_2 interaction with amine groups, likely *via* carbamate formation through zwitterionic intermediates.

In the fingerprint region (2600–1100 cm^{-1}), distinct bands provided further evidence of chemisorption. Peaks at 1713 and 1670 cm^{-1} correspond to C=O stretching of carbamic acid, while strong bands at 1552 and 1535 cm^{-1} indicate asymmetric stretching of COO^- and $RNHCOO^-$ in carbamate species.[45–49] Additional features at 1644 and 1470 cm^{-1} reflect NH_3^+ bending, and bands from 1500–1400 cm^{-1} include C–N stretching and N–H deformation, supporting diverse amine-CO_2 interactions.[45–47,49,50] A minor peak at 1365 cm^{-1} indicates limited bicarbonate formation. These chemisorption mechanisms are well aligned with previous literature.

A broad region between 1275–1221 cm^{-1} was assigned to C–N stretching of carbamate backbones, and a negative band at 2350 cm^{-1} reflected background subtraction of gaseous CO_2.

Overall, these results confirm that [TEAB][TEPA]$_2$ retains its chemisorption functionality after immobilization, primarily *via* carbamate and carbamic acid formation. Water assists this process by enabling proton transfer and minor bicarbonate generation, validating the liquid-to-solid transformation strategy for solid-like CO_2 adsorption.

Verification of composite structure and localization of [TEAB][TEPA]$_2$ within ZIF-8

To extend this strategy to other DES-MOF systems and enable the rational design of efficient composites in future studies, it is

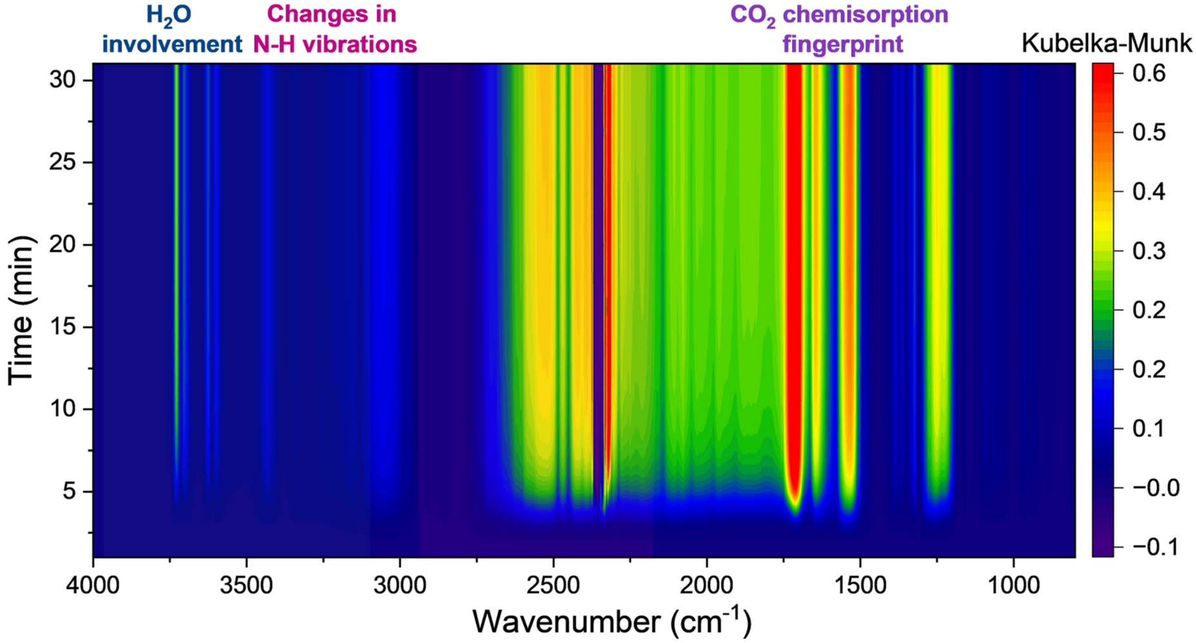

Fig. 7 *In situ* DRIFTS analysis of [TEAB][TEPA]$_2$@ZIF-8-56% under a binary CO_2/N_2 gas mixture (15/85, v/v). A 2D color map from 4000 to 800 cm^{-1} visualizing the temporal evolution of vibrational features. The total gas flow rate was maintained at 20 mL min^{-1}.

crucial to understand how [TEAB][TEPA]$_2$ behaves within the ZIF-8 framework—particularly whether the DES can partially infiltrate into the MOF's micropores and how such localization influences CO_2 capture.

As a first step, short-term CO_2 capture-release cycles were conducted on pristine ZIF-8 under the same conditions used for [TEAB][TEPA]$_2$@ZIF-8–56%—specifically, 15% CO_2 in N_2 at 25 °C—using TGA. As shown in Fig. S6, pristine ZIF-8 exhibited low CO_2 uptake (∼0.06 mmol g^{-1}) with negligible variation across cycles. In contrast, the composite maintained a markedly higher capacity (∼1.10 mmol g^{-1}) even after repeated cycles. When compared with the rapid performance degradation of [TEAB][TEPA]$_2$@alumina in Fig. 2, these results suggest possible interactions between the DES and the ZIF-8 framework, potentially involving partial pore infiltration.

In addition, to further support the possible infiltration of [TEAB][TEPA]$_2$ into the ZIF-8 framework, XPS analyses were conducted on both pristine ZIF-8 and the [TEAB][TEPA]$_2$@ZIF-8–56%, including depth profiling of the latter. Analysis of the outermost surface (0 min etch), presented in Fig. S7, revealed

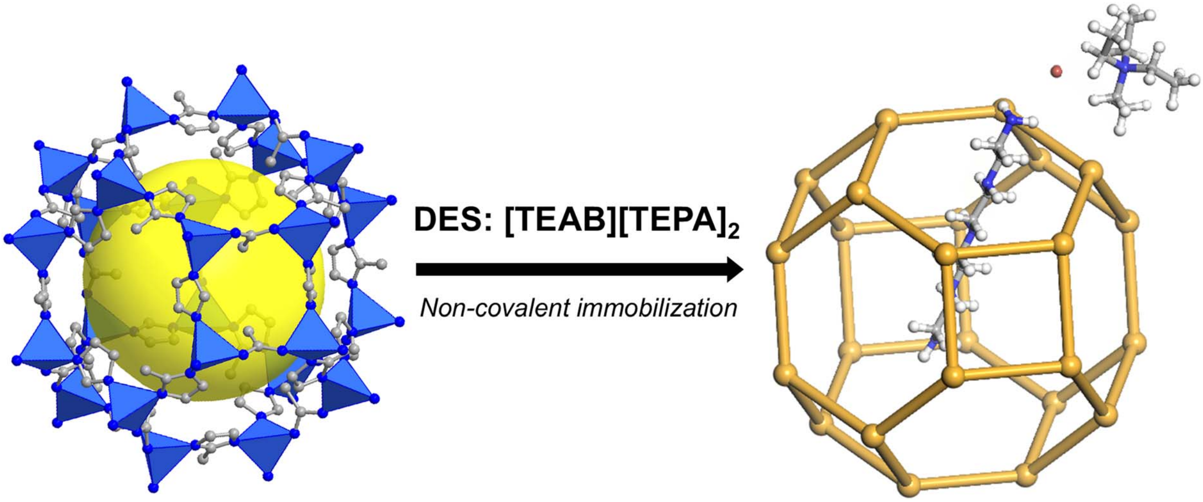

Scheme 1 Schematic illustration of the incorporation and proposed interaction of [TEAB][TEPA]$_2$ within the ZIF-8 framework *via* non-covalent immobilization. The left structure represents a ZIF-8 cage with its micropore volume (yellow sphere) and surrounding ZnN_4 tetrahedral units (blue), while the right structure shows [TEAB][TEPA]$_2$ molecules partially confined within the cage, emphasizing pore infiltration and host–guest interactions following DES loading.

characteristic peaks of the Zn lattice alongside size-induced defects, consistent with the heightened defect densities typically observed in nanocrystalline MOFs. Furthermore, the N 1 s region displayed additional signals indicative of primary and secondary amines from TEPA. As depth profiling proceeded, distinct shifts in the binding energies of the Zn $2p_{3/2}$, N 1s, Br 3d, and O 1s regions were observed, indicating depth-dependent chemical and electronic variations within the composite, as shown in Fig. 3(a). Notably, both the Zn $2p_{3/2}$ and N 1s regions showed clear peak splitting, with binding energy components shifting in opposite directions—downward for Zn $2p_{3/2}$ and upward for N 1s—suggesting the formation of Zn–N coordination bonds between TEPA amine groups and Zn^{2+} sites in the ZIF-8 framework. These opposing shifts reflect an increase in electron density around Zn and a decrease around coordinated nitrogen, consistent with donor–acceptor interactions. In addition, the composite showed a Br 3d signal—absent in pristine ZIF-8—confirming the presence of Br-containing $[TEAB][TEPA]_2$. The Br 3d region also showed a gradual shift toward lower binding energy with increased etching depth, possibly due to hydrogen bonding between Br^- and protonated amines or defects. Meanwhile, the O 1s signal faded with depth, suggesting water remained near the surface—likely excluded from the hydrophobic pores.[48]

Additionally, several analytical strategies reported in previous studies on liquid-MOF composites offer indirect support for the localization of DES in our system. For instance, FTIR peak shifts observed after composite formation have been cited as evidence for molecular interactions and pore infiltration in MOF-ionic liquid systems.[51,52] As shown in Fig. S8 and summarized in Table S2, $[TEAB][TEPA]_2$@ZIF-8–56% exhibited similar peak shift trends compared to those of its individual components. Moreover, new bands at 1350, 1333, and 1243 cm^{-1}, absent in both neat DES and ZIF-8, emerged upon composite formation. These are tentatively assigned to C–N stretching in secondary amines and CH_2/CH_3 bending, suggesting the formation of hydrogen bonds or weak coordination between $[TEAB][TEPA]_2$ and Zn^{2+} centers or defect sites in the ZIF-8 framework.

To further investigate $[TEAB][TEPA]_2$ localization, a washing experiment was designed based on the approach used by Zeeshan *et al.*, where dimethylformamide (DMF, kinetic diameter ∼5.5 Å)—which is unable to access ZIF-8 pores due to size and lack of affinity—was used to differentiate between pore-infiltrated and surface-deposited species.[53,54] Following this strategy, four distinct washing protocols were implemented in our study to evaluate the retention of $[TEAB][TEPA]_2$ within the composite: (1) rapid, involving immediate rinsing with 50 °C DMF; (2) light, consisting of three 10 minute soakings; (3) moderate, consisting of three 1 hour soakings; and (4) intensive, involving three soakings carried out over the course of a full day—all performed at 50 °C. FTIR spectra were collected for each washed sample to assess the presence of the DES phase. As highlighted in the blue-shaded region of Fig. S9, the key vibrational signatures of the DES were preserved across all washing conditions, comparable to those observed in the unwashed composite. This persistence suggests that $[TEAB][TEPA]_2$ is not merely adsorbed on the external surface but remains within the material, supporting the hypothesis of partial pore infiltration and/or strong interfacial retention. This conclusion is further supported by structural considerations. Although ZIF-8 possesses a nominal pore aperture of ∼3.4 Å, it is known to exhibit dynamic framework flexibility through linker rotation, enabling transient expansion that can accommodate linear molecules such as *n*-hexane (kinetic diameter ∼4.3 Å). Given TEPA's linear and conformationally flexible structure with multiple rotatable C–N bonds, it is plausible that TEPA can adopt an elongated conformation and align axially to partially access ZIF-8's pore channels. In contrast, bulkier molecules like DMF are excluded due to steric hindrance and lack of interaction with the hydrophobic framework, explaining their efficacy in removing surface-deposited species while leaving pore-infiltrated TEPA intact.

In parallel, prior studies have also pointed to decreases in PXRD peak intensity—especially the first diffraction peak—and reductions in textural properties (BET area and pore volume) as signs of liquid incorporation within MOF pores. Fig. S10, S11, and Table 1 present PXRD patterns (normalized to the intensity at $q = 9\ nm^{-1}$ for consistent comparison), pore size distribution curves, and N_2 sorption-derived textural properties for both pristine ZIF-8 and $[TEAB][TEPA]_2$@ZIF-8–56%. The composite shows a noticeable decline in the intensity of the first PXRD peak, as well as a significant drop in BET surface area and pore volume. While these changes are often interpreted as evidence of pore infiltration, they may also result from surface deposition and pore blocking by the DES. Accordingly, in this study, these metrics were considered only as supporting—rather than conclusive—evidence of DES incorporation.

Taken together, the results from TGA, XPS depth profiling, FTIR, N_2 isotherm and PXRD collectively suggest that the DES in $[TEAB][TEPA]_2$@ZIF-8 is not merely surface-deposited but is at least partially infiltrated into the ZIF-8 framework, where it interacts strongly with the host—particularly through the TEPA component. This interpretation aligns with the well-documented framework flexibility of ZIF-8: although its pore apertures are nominally ∼3.4 Å, the structure undergoes "gate-opening" *via* rotation of 2-methylimidazolate linkers, allowing accommodation of larger guest molecules.[54] For instance, ZIF-8 can readily admit linear hydrocarbons like *n*-hexane while excluding bulkier isomers such as cyclohexane.

Analogously, TEPA's linear and conformationally flexible structure—with multiple rotatable C–N bonds—likely enables partial penetration into ZIF-8's micropores. Once confined, its amine groups may potentially coordinate with internal Zn^{2+} centers or form hydrogen bonds with the framework's nitrogen sites. In contrast, the bulkier tetraethylammonium (TEAB) cations and water molecules are largely excluded from the pores due to steric hindrance and the hydrophobic interior of ZIF-8. Supporting this, Qiu *et al.* reported that amphiphilic TEPA molecules can be immobilized within ZIF-8 pores *via* hydrophobic interactions between their alkyl chains and the nonpolar pore walls.[55]

As shown in Scheme 1, the proposed structural arrangement highlights the partitioning behavior of the DES components within the ZIF-8 framework. In this model, [TEAB][TEPA]$_2$ undergoes spatial separation where TEPA penetrates and binds within the micropores, while TEAB predominantly resides on the external surface. This selective partitioning behavior provides a coherent explanation for the spectroscopic and structural observations obtained. Specifically, the thermogravimetric behavior, enhanced CO_2 uptake during TGA cycling, FTIR band shifts associated with Zn–N bonding, residual DES signals after DMF washing, and distinct XPS features at varying depths all point toward TEPA's partial pore infiltration and strong interaction with the internal surface of the ZIF-8 framework. The visualization in Scheme 1 further supports this interpretation by illustrating how the DES molecules interact with both the pore interior and exterior of the MOF. Collectively, these findings suggest that a portion of the DES is immobilized inside the ZIF-8 structure in intimate contact with the host, thereby validating the liquid-to-solid functional transformation strategy employed in this study.

Conclusions

In response to the urgent need for durable carbon capture technologies, we developed a solid–liquid hybrid system by immobilizing the deep eutectic solvent (DES) [TEAB][TEPA]$_2$ onto various solid supports to exploit the chemisorptive properties of the DES in solid-state applications. Under identical synthesis conditions, FTIR and PXRD confirmed successful DES immobilization and structural retention. Among the materials tested, nanosized ZIF-8- and alumina-based composites showed promising CO_2 uptake at 298 K, and TGA cycling (>100 capture–release cycles) was used to assess durability. While the CO_2 capacity of the alumina composite declined toward that of pristine alumina, the ZIF-8 composite maintained stable performance even after extended cycling and was selected for further investigation.

The optimized [TEAB][TEPA]$_2$@ZIF-8–56% composite exhibited superior uptake capacities of 0.59, 0.96, and 1.48 mmol g^{-1} at 0.4 mbar, 0.01 bar, and 0.15 bar, respectively—representing enhancements of over 16-fold and 13.5-fold at 0.01 and 0.15 bar relative to pristine ZIF-8. Breakthrough experiments under simulated dry and humid CO_2/N_2 conditions confirmed the composite's robust dynamic adsorption behavior, demonstrating that the immobilized DES phase retains its reactivity even in humid environments.

Mechanistic analysis by *in situ* DRIFTS verified that the DES's chemisorptive functionality was preserved after immobilization, achieving the goal of retaining liquid-like reactivity in a solid matrix. Complementary FTIR, PXRD, N_2 physisorption, and XPS depth profiling provided evidence of partial DES confinement within ZIF-8 and strong host–guest interactions. Depth-dependent spectral shifts, persistence of DES after washing, and reduced N_2 accessibility collectively support intimate DES integration in the ZIF-8 framework.

The notable performance of the ZIF-8 composite may arise from a combination of factors, such as its microporosity, which could allow partial confinement of the DES; potential surface interactions between the framework and DES molecules; and its nanoscale morphology, which may facilitate improved mass transfer. Overall, this study suggests a promising approach for the development of regenerable, solid-state carbon capture materials that aim to combine advantages of liquid-phase systems with the durability and scalability of solid supports.

Author contributions

Yunsung Yoo: conceptualization, methodology, investigation, validation, visualization, data curation, writing – original draft. Xiaoliang Wang: investigation, visualization, validation, writing – review & editing. Haomiao Xie: validation, visualization. Geun-Ho Han: investigation, visualization, validation. Ji-Yoon Song: investigation. Milad Ahmadi Khoshooei: investigation. Kent O. Kirlikovali: writing – review & editing. Justin M. Notestein: writing – review & editing. Edward H. Sargent: writing – review & editing. Omar K. Farha: writing – review & editing, methodology, supervision, validation, visualization, resources, funding acquisition.

Conflicts of interest

There are no conflicts to declare.

Data availability

The data supporting this article have been included as part of the supplementary information (SI). Supplementary information: additional experimental details, characterization data (FTIR, PXRD, SEM-EDS, TGA, XPS, and ICP-OES), adsorption isotherm fitting procedures and parameters, breakthrough curves, *in situ* DRIFTS spectra, and figures and tables supporting the main text. See DOI: https://doi.org/10.1039/d5ta07025b.

Acknowledgements

O.K.F. gratefully acknowledges support from the Catalyst Design for Decarbonization Center, an Energy Frontier Research Center funded by the U.S. Department of Energy, Office of Science, Basic Energy Sciences (DE-SC0023383), the Trienens Institute for Sustainability and Energy at Northwestern University, and Boeing. This work made use of the Crystallography and Physical Characterization facilities at the Integrated Molecular Structure Education and Research Center (IMSERC, RRID: SCR_017874), as well as the EPIC (RRID: SCR_026361) and Keck-II (RRID: SCR_026360) facilities of the NUANCE Center at Northwestern University. These facilities have received support from the Soft and Hybrid Nanotechnology Experimental (SHyNE) Resource (NSF ECCS-2025633), the International Institute for Nanotechnology (IIN), Northwestern's Materials Research Science and Engineering Center (MRSEC, NSF DMR-2308691), and Northwestern University. We also thank Julian S. Magdalenski (Northwestern University) for his assistance with sample preparation.

Notes and references

1 H. McLaughlin, A. A. Littlefield, M. Menefee, A. Kinzer, T. Hull, B. K. Sovacool, M. D. Bazilian, J. Kim and S. Griffiths, *Renew. Sustain. Energy Rev.*, 2023, **177**, 113215.

2 B. K. Sovacool, D. F. Del Rio, K. Herman, M. Iskandarova, J. M. Uratani and S. Griffiths, *Energy Environ. Sci.*, 2024, **17**(10), 3523–3569.

3 S. Chen, J. Liu, Q. Zhang, F. Teng and B. C. McLellan, *Renew. Sustain. Energy Rev.*, 2022, **167**, 112537.

4 W. Gao, S. Liang, R. Wang, Q. Jiang, Y. Zhang, Q. Zheng, B. Xie, C. Y. Toe, X. Zhu and J. Wang, *Chem. Soc. Rev.*, 2020, **49**, 8584–8686.

5 X. Zhu, W. Xie, J. Wu, Y. Miao, C. Xiang, C. Chen, B. Ge, Z. Gan, F. Yang and M. Zhang, *Chem. Soc. Rev.*, 2022, **51**, 6574–6651.

6 K. Madhu, S. Pauliuk, S. Dhathri and F. Creutzig, *Nat. Energy*, 2021, **6**, 1035–1044.

7 S. Kar, D. Kim, A. Bin Mohamad Annuar, B. B. Sarma, M. Stanton, E. Lam, S. Bhattacharjee, S. Karak, H. F. Greer and E. Reisner, *Nat. Energy*, 2025, 1–12.

8 M. Erans, E. S. Sanz-Pérez, D. P. Hanak, Z. Clulow, D. M. Reiner and G. A. Mutch, *Energy Environ. Sci.*, 2022, **15**, 1360–1405.

9 S. Bose, D. Sengupta, T. M. Rayder, X. Wang, K. O. Kirlikovali, A. K. Sekizkardes, T. Islamoglu and O. K. Farha, *Adv. Funct. Mater.*, 2024, **34**, 2307478.

10 N. Von Der Assen, L. J. Müller, A. Steingrube, P. Voll and A. Bardow, *Environ. Sci. Technol.*, 2016, **50**, 1093–1101.

11 P. R. Rochedo and A. Szklo, *Appl. Energy*, 2013, **108**, 383–391.

12 M. C. Freyman, Z. Huang, D. Ravikumar, E. B. Duoss, Y. Li, S. E. Baker, S. H. Pang and J. A. Schaidle, *Joule*, 2023, **7**, 631–651.

13 G. T. Rochelle, *Science*, 2009, **325**, 1652–1654.

14 F. Meng, Y. Meng, T. Ju, S. Han, L. Lin and J. Jiang, *Renew. Sustain. Energy Rev.*, 2022, **168**, 112902.

15 D. J. Heldebrant, P. K. Koech, V.-A. Glezakou, R. Rousseau, D. Malhotra and D. C. Cantu, *Chem. Rev.*, 2017, **117**, 9594–9624.

16 X. Shi, H. Xiao, H. Azarabadi, J. Song, X. Wu, X. Chen and K. S. Lackner, *Angew. Chem., Int. Ed.*, 2020, **59**, 6984–7006.

17 S. Zeng, X. Zhang, L. Bai, X. Zhang, H. Wang, J. Wang, D. Bao, M. Li, X. Liu and S. Zhang, *Chem. Rev.*, 2017, **117**, 9625–9673.

18 M. Aghaie, N. Rezaei and S. Zendehboudi, *Renew. Sustain. Energy Rev.*, 2018, **96**, 502–525.

19 B. B. Hansen, S. Spittle, B. Chen, D. Poe, Y. Zhang, J. M. Klein, A. Horton, L. Adhikari, T. Zelovich and B. W. Doherty, *Chem. Rev.*, 2020, **121**, 1232–1285.

20 S. Dongare, M. Zeeshan, A. S. Aydogdu, R. Dikki, S. F. Kurtoğlu-Öztulum, O. K. Coskun, M. Muñoz, A. Banerjee, M. Gautam and R. D. Ross, *Chem. Soc. Rev.*, 2024, **53**, 8563–8631.

21 A. Azzouz and M. Hayyan, *Chem.–Eng. J.*, 2023, **468**, 143563.

22 E. L. Smith, A. P. Abbott and K. S. Ryder, *Chem. Rev.*, 2014, **114**, 11060–11082.

23 S. Sarmad, J. P. Mikkola and X. Ji, *ChemSusChem*, 2017, **10**, 324–352.

24 S. Kwon, M. Park, J. Jo, Y. Yoo and D. Kang, *Chem.–Eng. J.*, 2025, **503**, 158172.

25 J. Ju, D. Choi, S. Cho, Y. Yoo and D. Kang, *Chem.–Eng. J.*, 2024, **496**, 153922.

26 M. Park, S. Kwon, J. Park, J. Jo, Y. Yoo and D. Kang, *Chem.–Eng. J.*, 2023, **468**, 143552.

27 J. Ruan, L. Chen and Z. Qi, *Green Chem.*, 2023, **25**, 8328–8348.

28 F. Yang, T. Ge, X. Zhu, J. Wu and R. Wang, *Sep. Purif. Technol.*, 2022, **287**, 120535.

29 F. Yang, J. Wu, X. Zhu, T. Ge and R. Wang, *Chem.–Eng. J.*, 2021, **410**, 128322.

30 F. A. Philip and A. Henni, *Microporous Mesoporous Mater.*, 2022, **330**, 111580.

31 X. Li, K. Chen, R. Guo and Z. Wei, *Chem. Rev.*, 2023, **123**, 10432–10467.

32 S. Gaikwad, Y. Kim, R. Gaikwad and S. Han, *J. Environ. Chem. Eng.*, 2021, **9**, 105523.

33 A. U. Khan, O. Samuel, M. H. D. Othman, M. Younas, R. Kamaludin, M. H. Puteh, T. A. Kurniawan, K. Y. Wong, F. Kadirkhan and N. Yoshida, *Sep. Purif. Technol.*, 2024, **347**, 127511.

34 M. Ding, R. W. Flaig, H.-L. Jiang and O. M. Yaghi, *Chem. Soc. Rev.*, 2019, **48**, 2783–2828.

35 S. Shang, Z. Tao, C. Yang, A. Hanif, L. Li, D. C. Tsang, Q. Gu and J. Shang, *Chem.–Eng. J.*, 2020, **393**, 124666.

36 S. K. Gebremariam, A. M. Varghese, S. Ehrling, Y. Al Wahedi, A. AlHajaj, L. F. Dumée and G. N. Karanikolos, *ACS Appl. Mater. Interfaces*, 2024, **16**, 50785–50799.

37 M. Lalehchini, A. Mohajeri, M. M. A. Nikje and M. Rezapour, *Microporous Mesoporous Mater.*, 2024, **378**, 113242.

38 Y. Ban, Z. Li, Y. Li, Y. Peng, H. Jin, W. Jiao, A. Guo, P. Wang, Q. Yang and C. Zhong, *Angew. Chem., Int. Ed.*, 2015, **54**, 15483–15487.

39 M. Zunita, R. Hastuti, A. Alamsyah, K. Khoiruddin and I. Wenten, *Separ. Purif. Rev.*, 2022, **51**, 261–280.

40 M. Erkartal, U. Erkilic, B. Tam, H. Usta, O. Yazaydin, J. T. Hupp, O. K. Farha and U. Sen, *Chem. Commun.*, 2017, **53**, 2028–2031.

41 J. Cravillon, S. Münzer, S.-J. Lohmeier, A. Feldhoff, K. Huber and M. Wiebcke, *Chem. Mater.*, 2009, **21**, 1410–1412.

42 P. Agbo, K. An, S. E. Baker, J. Cross, L. Kreibe, W. Li, C. Myers, S. H. Pang, H. T. Schaef and J. A. Schaidle, 2024.

43 J. Zhang, J. Zhu, L. Kang, Q. Zhang, L. Liu, F. Guo, K. Li, J. Feng, L. Xia and L. Lv, *Energy Environ. Sci.*, 2023, **16**, 6015–6025.

44 C. Belver, C. Breen, F. Clegg, C. E. Fernandes and M. A. Vicente, *Langmuir*, 2005, **21**, 2129–2136.

45 G. Rim, P. Priyadarshini, M. Song, Y. Wang, A. Bai, M. J. Realff, R. P. Lively and C. W. Jones, *J. Am. Chem. Soc.*, 2023, **145**, 7190–7204.

46 G. S. Foo, J. J. Lee, C. H. Chen, S. E. Hayes, C. Sievers and C. W. Jones, *ChemSusChem*, 2017, **10**, 266–276.

47 W. C. Wilfong, C. S. Srikanth and S. S. Chuang, *ACS Appl. Mater. Interfaces*, 2014, **6**, 13617–13626.

48 H. J. Esfahani, A. Ghaemi and S. Shahhosseini, *Sci. Rep.*, 2024, **14**, 18871.

49 J. Yu and S. S. Chuang, *Energy Fuels*, 2016, **30**, 7579–7587.

50 X. Wang, V. Schwartz, J. C. Clark, X. Ma, S. H. Overbury, X. Xu and C. Song, *J. Phys. Chem. C*, 2009, **113**, 7260–7268.

51 B. Koyuturk, C. Altintas, F. P. Kinik, S. Keskin and A. Uzun, *J. Phys. Chem. C*, 2017, **121**, 10370–10381.

52 F. P. Kinik, C. Altintas, V. Balci, B. Koyuturk, A. Uzun and S. Keskin, *ACS Appl. Mater. Interfaces*, 2016, **8**, 30992–31005.

53 M. Zeeshan, V. Nozari, M. B. Yagci, T. Isık, U. Unal, V. Ortalan, S. Keskin and A. Uzun, *J. Am. Chem. Soc.*, 2018, **140**, 10113–10116.

54 K. Zhang, R. P. Lively, C. Zhang, R. R. Chance, W. J. Koros, D. S. Sholl and S. Nair, *J. Phys. Chem. Lett.*, 2013, **4**, 3618–3622.

55 Q. Ren, J.-W. Yu, H.-B. Luo, J. Zhang, L. Wang and X.-M. Ren, *Inorg. Chem.*, 2019, **58**, 14693–14700.